Effect of resultant force direction in machining of single crystal (100)Ge

Effect of resultant force direction in machining of single crystal (100)Ge

M. Tunesi

School of Mechanical and Aerospace Engineering

Oklahoma State University, Stillwater, OK 74078

email: michele.tunesi@okstate.edu

Current address:

Department of Management and Production Engineering, Politecnico di Torino, Corso Duca degli Abruzzi 24, 10129 Turin, Italy

michele.tunesi@polito.it

E. Lawing

Department of Mechanical Engineering

University of North Carolina at Charlotte, Charlotte, NC 28223

email: elawing4@charlotte.edu

C. Estes

Moore Nanotechnology Systems

6510 Northpark Blvd, Charlotte, NC 28216

email: colton.estes@nanotechsys.com

J. Gasson

Moore Nanotechnology Systems

6510 Northpark Blvd, Charlotte, NC 28216

email: john.gasson@nanotechsys.com

M.A. Davies

Moore Nanotechnology Systems

6510 Northpark Blvd, Charlotte, NC 28216

Department of Mechanical Engineering

University of North Carolina at Charlotte, Charlotte, NC 28223

Email: matt.davies@nanotechsys.com

D.A. Lucca[1]
School of Mechanical and Aerospace Engineering
Oklahoma State University, Stillwater, OK 74078
email: lucca@okstate.edu

Highlights

- Resultant force direction influences surface fracture patterns in single crystal (100)Ge during on-axis single point diamond turning
- The ratio $\left[\frac{S_f}{F_f}\right]^*$ was used to quantify the relative favorability of slip and fracture based on crystallographic orientation and resultant force angle
- The <110> direction is predicted to generate fracture when the resultant force angle is less than 40°
- Both the <110> and <100> directions are predicted to generate fracture when the resultant force angle is between 40° and 55°
- The <100> direction is predicted to generate fracture when the resultant force angle is larger than 55°

Abstract

On-axis single point diamond turning experiments were conducted on (100)Ge to investigate the relation between the direction of the resultant force and the surface topography. This was done by measuring cutting and thrust forces for feedrates ranging from 0.3 μm/rev to 12 μm/rev. The geometrical relation between the resultant force, slip

[1] Corresponding author

systems and fracture systems was investigated using the Schmid factor S_f and the fracture factor F_f. Their ratio $\left[\frac{S_f}{F_f}\right]^*$ was used to identify the cutting directions that were more favorable for slip and fracture. The surface topography, measured by AFM, corresponded with the $\left[\frac{S_f}{F_f}\right]^*$ prediction. Three regimes were identified on (100)Ge depending on the resultant force angle φ. When φ < 40°, fracture is predicted for cutting directions along <110>. When 40° < φ < 55, fracture is predicted for cutting directions along both <100> and <110>. When φ > 55°, fracture is predicted for cutting directions along <100>. The study of $\left[\frac{S_f}{F_f}\right]^*$ for the Ge lattice indicates that fracture is the most favorable when the force is aligned with the <110> and <111> direction families. This study shows that the slip and fracture systems can be used in machining of Ge in order to suppress fracture and favor shear deformation.

Keywords

Single point diamond turning, Germanium, Single crystal, Deformation, Fracture

1 Introduction

Single crystal Ge is used in the production of optical components in imaging systems and thermal sensors as a result of its broad optical transparency in the infrared [1,2]. It has near complete optical transmission for wavelengths ranging from 1.9 μm to 14 μm at room temperature [2,3]. Large Ge specimens can be produced using the Czochralski method with excellent crystal quality and known lattice orientation [4]. The bulk material can then be machined by single point diamond turning to obtain surfaces ranging from flats to freeforms [5]. Because of the brittle nature of Ge, the parameters used in diamond machining are often conservative to minimize resulting lattice disorder and the introduction of fracture on and below the surface. This approach limits the manufacturing efficiency of Ge optics. A more detailed study of the lattice response to single point diamond turning is required to optimize the process and to better understand the mechanisms governing material removal in single crystal Ge.

The final surface topography of machined Ge is determined by the relative orientation of the cutting direction and the crystal lattice. In the seminal study by Nakasuji [6], it was established that some cutting directions generate brittle fracture during on-axis turning, while other cutting directions do not under the same machining conditions. Due to the symmetry of the single crystal lattice and the geometry of on-axis turning, the final surface topography consists of circular sectors with pronounced surface fracture, referred to as lobes. The extent of fracture is directly correlated with the feedrate, as observed in (100)Ge and (111)Ge, viz., higher feedrates result in uniformly distributed pits that are larger and

deeper with increasing feedrate [7,8]. Even when the optimal cutting direction is isolated by off-axis turning, the feedrate has been shown to affect both the surface topography and the resulting residual stress [9]. More recent on-axis single point diamond turning experiments on (100)Ge have shown that the brittle fracture density is also affected by the cutting speed when the feedrate is maintained constant [10–12]. As the cutting speed increased, fracture pit size, depth and density decreased. In those experiments, three distinct lobes were found on the surface when the cutting speed was below 4 m/s, two dominated by brittle fracture and corresponding to the <100> and <110> cutting direction families, and one in between these cutting directions where fracture was minimized or absent.

In a recent study focused on the resultant force direction in single point diamond turning of (111)CaF_2, it was found that the Schmid factor and the fracture factor could explain the resulting surface topography and the mechanism behind fracture for certain cutting directions [13]. The respective maxima of the factors were combined in a parameter $\left[\frac{S_f}{F_f}\right]^*$, that indicates the propensity of the crystal under a given load to favor shear deformation or brittle fracture. The ratio $\left[\frac{S_f}{F_f}\right]^*$ was used to explain conflicting results reported in the literature, by highlighting how the response of (111)CaF_2 changes as a function of the resultant force angle for the same cutting direction families. The analysis of the Schmid factor and fracture factor has been used also to explain the resulting topography in plunge cut experiments on different surfaces of single crystal sapphire [14,15]. It was found that

crack morphology and plastic deformation could be explained by the geometrical relation of the resultant force with the slip systems and fracture systems.

The objective of this study is to determine whether when machining single crystal Ge with single point diamond turning, the surface topography is governed by the slip system and fracture system orientation. This is pursued by using a similar approach that was used for on-axis turning of CaF_2. A single crystal Ge specimen with a (100) surface orientation was machined at feedrates ranging from 0.3 μm/rev to 10 μm/rev while cutting and thrust forces were measured. The surface topography was characterized by AFM. The resultant force angle was used to compute the Schmid factor, fracture factor, and $\left[\frac{S_f}{F_f}\right]^*$. Analysis of the factors was used to explain the observed surface features and the specific force directions that promote fracture in single crystal Ge.

2 Materials and Methods

2.1 Specimen machining

On-axis single point diamond turning experiments were performed on a 5-axis Nanotech 250 UPL-MP from Moore Nanotechnology Systems. A single crystal Ge specimen with (100) surface orientation, a diameter of 50 mm and thickness of 5 mm was used. The specimens were produced by Lattice Materials and were oriented with a fiduciary mark indicating the <100> radial direction. A round nose single crystal diamond tool, manufactured by K&Y Diamond, was used. The tool radius was 1.008 mm, and the rake angle was -25°. The tool edge radius was measured to be between 75 nm and 125 nm. The

tool was aligned and positioned using the machine integrated optical tool set station. The machining setup is shown in Fig. 1(a, b). The specimen was first mounted on the specimen holder using wax that crystallizes at room temperature. Figure 1(c, d) shows a schematic of the tool in relation to the workpiece. The specimen was initially machined with a 10 μm depth of cut and a feedrate of 0.3 μm/rev to remove any tilt introduced during mounting. The machining parameters were chosen conservatively based on previous Ge machining experiments performed by the authors in which the surface and subsurface integrity was measured by Raman spectroscopy, RBS channeling and AFM [7]. The rotational speed was 2000 rpm and was maintained constant. The tool was positioned 200 μm below the spindle axis to avoid turning the specimen to center. This left a 400 μm diameter land at the center of the specimen. For the turning experiments, 8 bands with a width of 2 mm each were machined. The depth of cut was 10 μm and the feedrate was varied from 0.3 μm/rev to 12 μm/rev. The cutting speed was maintained constant at 4 m/s on each band by adjusting the rotational speed continuously through the machine controller. The turning experiments were performed from the outside radius of 25 mm to 9 mm from the spindle center. The specimen preparation and experimental parameters are reported in Table 1.

Cutting (F_C) and thrust (F_T) forces were measured using a Kistler 9256C1 piezoelectric dynamometer and a Kistler 5167A charge amplifier during on-axis machining, as shown in Fig. 1(b). The tool was mounted directly on the dynamometer, and the measurement frequency was 10 kHz. The feed force (F_F) was at least one order of magnitude smaller than F_C and F_T, so it was not considered in the calculations. To correct for dynamometer

drift, a first order polynomial was subtracted from the raw data. The fitting of the polynomial was performed using approximately 2 s of data before tool contact and after tool retraction.

2.2 Calculation of $[S_f/F_f]^*$ for on-axis turning

To determine the effect of the resultant force direction on the slip and fracture systems, a vector space representing all possible cutting directions and resultant force angles was generated. Starting from the [011] direction within the (100) plane, a set of directions was computed through two transformations performed by rotation tensors, one around the direction normal to the surface and then one into the surface plane. This produced a set of vectors $\hat{t}(\delta, \varphi)$ that mapped all possible force directions as a function of the angles δ and φ, representing the cutting direction and resultant force angle respectively. In this geometry the resultant force angle is between surface of the specimen and the resultant force. The rotations were calculated in 1° increments. More details on this method and the equations used can be found elsewhere [16].

The slip behavior of single crystal Ge was analyzed by evaluating the Schmid factor (S_f), which is the ratio of the resolved shear stress to the applied stress required to activate the slip system [17]. The {111}<110> slip systems were considered, as listed in Table 2, which are the only slip systems available at room temperature [18,19]. For each direction in the vector space $\hat{t}$, the angle α between the force direction and the slip plane normal, and the angle β between the force direction and the slip direction, were computed. S_f for the i^{th} slip system was then calculated using Eq. 1,

$$S_{f,i}(\delta,\varphi) = \cos(\alpha_i(\delta,\varphi))\cos(\beta_i(\delta,\varphi)) \quad (1)$$

Fracture behavior was similarly analyzed using the fracture factor (F_f), which is the ratio of the critical fracture stress to the applied stress. Single crystal Ge has been shown to fracture on the {111} family of planes [20]. Additionally, single crystal Si, which has the same crystal structure as Ge, has been shown to fracture on the {110} planes [21]. Since the {110} family of planes of Ge has a comparable surface energy to that of the {111} family [22], both were considered for the F_f calculation. To estimate the relative stress required to cause fracture on the two plane families, the elastic moduli reported by Wortman et al. were used [23]. The elastic moduli are 153 GPa and 142 GPa for the {111} and {110} families respectively, resulting in an estimated ratio of their critical stresses of 0.93. The fracture systems considered are listed in Table 2. For each direction in the vector space $\hat{t}$, the angle γ between the force direction and the normal to the fracture plane was calculated. The F_f for each plane was then computed using Eq. 2,

$$F_{f,i}(\delta,\varphi) = \cos^2(\gamma_i(\delta,\varphi)) \quad (2)$$

Using the sets of S_f and F_f, the slip system and fracture system with the highest value were compared as a function of cutting direction and resultant force angle, using Eq. 3,

$$\left[\frac{S_f}{F_f}\right]^*(\delta,\varphi) = \max(S_{f,i}(\delta,\varphi)) \Big/ \max(F_{f,i}(\delta,\varphi)) \quad (3)$$

2.3 Calculation of $[S_f/F_f]^*$ for a general force direction

The algorithm used for the calculation of S_f, F_f and $\left[\frac{S_f}{F_f}\right]^*$ for the case of turning was adapted to study the factors for all possible directions. In order to generate a set of directions that uniformly sampled the 3D space, a MATLAB toolbox was used [24]. The toolbox enables the approximation of a sphere of radius 1 by generating a fine triangular surface mesh based on the progressive subdivision of an icosahedron, as shown in Fig. 2. The coordinates of the points are then used as the set of directions $\hat{t}$ for which the factors are computed. The coordinates are meshed to generate the sphere tessellated by triangles. Each vertex represents a direction of the set $\hat{t}$.

With the set of directions generated, the angle between them and the slip/fracture systems are computed as previously shown. The slip system and fracture system that require the least stress to activate are selected using Eqs. 4 and 5 for each element of $\hat{t}$,

$$S_f(\hat{t}) = \max_i \left[S_{f,i}(\hat{t})\right] \tag{4}$$

$$F_f(\hat{t}) = \max_i \left[F_{f,i}(\hat{t})\right] \tag{5}$$

$\left[\frac{S_f}{F_f}\right]^*$ is then computed using Eq. 3.

A color scale is used to show the relative values of the factors for all possible force directions. The color on the faces of the tessellation is calculated by interpolating the values of the three vertexes where S_f, F_f and $\left[\frac{S_f}{F_f}\right]^*$ are calculated.

3 Results and Discussion

3.1 Surface topography

On-axis machining produced radial lobes with visible fracture, as shown in the optical image and the schematic in Fig. 3(a, b). In the picture the lobes have a hazy appearance and are marked by arrows. The most pronounced fracture appeared along the <100> cutting direction, shown in red, while a second, less densely fractured lobe was centered near the <110> direction, shown in yellow. As the feedrate decreased, both the size and visibility of these lobes diminished, eventually becoming undistinguishable from the rest of the specimen.

The topography was investigated by measuring areas of variable size depending on the feedrate, as shown in Fig. 4. The scan size of the AFM measurement was equal to or larger than three times the feedrate, in order to include several passes of the tool in the same image. The measurements were performed at the center of each machined band and for three cutting direction families: <100>, <110> and in between these two directions, approximately <210>. Tool marks were observed on all surfaces and corresponded to the nominal feedrate. Fracture was found in a mixture of 5 μm or smaller pits for the <100> cutting direction family when the feedrate was equal to or larger than 6 μm/rev. The fracture density increased with the feedrate and covered most of the surface at 12 μm/rev. Below 6 μm/rev only tool marks were distinguishable on the surface. Smaller and substantially less dense fracture was found for the <110> cutting direction family when the feedrate was 8 μm/rev or higher. For the <210> cutting direction family fracture was only present when the feedrate was 10 μm/rev or 12 μm/rev.

3.2 Effect of force direction on the surface topography

The cutting and thrust forces for one full revolution of the specimen machined by on-axis turning resulted in four oscillations per revolution that had the same phase, as shown in Fig. 5. The oscillations are associated with the tool traversing the lobes centered along the <100> cutting direction, with the fourfold symmetry that is expected on the (100) plane. For all feedrates except 0.3 μm/rev the force was near its maximum for most of the revolution, while the minimum was reached with a steep drop and recovery in force. The maximum of the force is associated with the large areas centered along the <110> cutting direction family. The minimum of the force is associated with the fracture that occurs along the <100> cutting direction family. To calculate representative values, the minimum, mean, and maximum of the forces were calculated from the data of 20 revolutions at the center of each band. The three values are summarized in Fig. 6. The cutting force increased from 0.3 μm/rev and after 4 μm/rev the average cutting force was approximately constant with feedrate. The thrust force decreased monotonically from 2 μm/rev.

The resultant force angle decreased monotonically with increasing feedrate, as shown in Fig. 7. The resultant force angle decreased steeply from 84° at 0.3 μm/rev to 67° at 2 μm/rev, then continued to decrease more gradually to 55° at 12 μm/rev. The small difference between minimum and maximum values at each feedrate indicates that the resultant force angle settles around a constant value throughout the rotation, and that the values reported are representative for all cutting directions.

S_f, F_f, and $\left[\frac{S_f}{F_f}\right]^*$ were computed for a range of resultant force angles from 55° to 65° and are shown in Fig. 8. This resultant force angle range is representative of the conditions

found in the experiments of this study. As the resultant force angle increases, S_f separates the slip systems into two sets: one with S_f that is increasing toward the theoretical maximum of 0.5, and one with values decreasing toward zero. The maximum value of S_f is found approximately 10° to 15° off the <100> cutting direction family, both clockwise and counterclockwise. The minimum value occurs when the cutting direction belongs to the <110> direction family. For F_f, the values decrease as the resultant angle increases. The maximum F_f occurs for the <100> direction family while the minimum occurs for the <110> direction family. For a resultant force angle of 55°, the {110} fracture system requires less stress to cause fracture when compared to the {111} fracture system.

The ratio $\left[\frac{S_f}{F_f}\right]^*$ is shown to have four or eight oscillations per revolution depending on the resultant force angle. As the resultant force angle increases, $\left[\frac{S_f}{F_f}\right]^*$ increases, which predicts a shift toward a more favorable condition for slip when compared to fracture. The {110} fracture system maximum for a resultant force angle of 55° results in a local minimum in $\left[\frac{S_f}{F_f}\right]^*$ for the <110> cutting direction family, which predicts less stress to activate fracture for those cutting directions.

Using the complete dataset of $\left[\frac{S_f}{F_f}\right]^*$, a 3D surface was generated as shown in Fig. 9(a). In the figure, a plane parallel to the cutting direction axis results in $\left[\frac{S_f}{F_f}\right]^*$ calculated for a given resultant force angle, as shown in the plots of Fig. 9(b) for angles of 55°, 60° and 65°. The 3D surface can be qualitatively divided into several sections. For the resultant force angle

range obtained for the experiments, the absolute minimum of $\left[\frac{S_f}{F_f}\right]^*$ always occurs for the <100> cutting direction. This is consistent with the AFM measurements shown in Fig. 4, where the largest and most dense fracture is found for the <100> direction family. As the feedrate decreases, the resultant force rotates into the surface as the angle increases and fracture decreases, consistent with the prediction of $\left[\frac{S_f}{F_f}\right]^*$ which steadily increases. Considering the <110> cutting direction, $\left[\frac{S_f}{F_f}\right]^*$ has a local minimum when the resultant force angle is 55°, which becomes the absolute maximum as the resultant force angle increases. This is also consistent with the AFM measurement of Fig. 4, when machining with a feedrate of 12 μm/rev, the fracture appears to marginally increase with respect to the nearby <210> direction. Decreasing the feedrate rotates the resultant force into the surface and <110> and <210> appear to be similar. As the resultant force angle increases beyond 65° there is a monotonic increase in $\left[\frac{S_f}{F_f}\right]^*$, as shown in the 3D surface of Fig. 9(a), which predicts that fracture should decrease and eventually disappear.

For smaller resultant force angles the behavior of (100)Ge is predicted to change. Figure 10 shows S_f, F_f, and $\left[\frac{S_f}{F_f}\right]^*$ for a resultant force angle ranging from 35° to 45°, and the 3D surface of $\left[\frac{S_f}{F_f}\right]^*$ is shown in Fig. 11. Considering a resultant force angle of 45°, both the <100> and <110> cutting direction families result in a minimum for $\left[\frac{S_f}{F_f}\right]^*$ that is comparable in magnitude. This predicts that two lobes with fracture should be present on

the surface, with different sizes based on how rapidly $\left[\frac{S_f}{F_f}\right]^*$ changes with the cutting direction. Evidence of this behavior was found in studies focused on the effect of speed when turning (100)Ge [10,11]. At the lower end of the cutting speed range, the resultant force angle was approximately 45°. In that study, two lobes with increased fracture were found, referred to as the primary and secondary lobes. The size varied consistently with the changes of $\left[\frac{S_f}{F_f}\right]^*$.

For a 35° resultant force angle, a third behavior of (100)Ge is predicted. The absolute minimum in $\left[\frac{S_f}{F_f}\right]^*$ is found for the <110> cutting direction family, while there is a local minimum relatively close to the $\left[\frac{S_f}{F_f}\right]^*$ maximum for the <100> cutting direction family. These predictions agree with the surface topography reported by Nakasuji for turned (100)Ge [6], although the corresponding resultant force angles were not explicitly reported. Considering the behavior of $\left[\frac{S_f}{F_f}\right]^*$ with respect to the resultant force angle, it is predicted that depending on the force direction obtained during machining, the cutting direction that generates fracture on the surface could change from <100> to <110>.

3.3 Generalized behavior of force direction on single crystal Ge

S_f, F_f and $\left[\frac{S_f}{F_f}\right]^*$ were computed for the Ge lattice using a spherical plot and are shown in Fig. 12. In the figure, each point on the sphere corresponds to a resultant force direction,

defined by the point's coordinates. The color indicates the value of S_f, F_f and $\left[\frac{S_f}{F_f}\right]^*$, mapped on a scale from blue to red for the minimum and maximum values, respectively. All slip and fracture systems were considered in the calculation. It was found that for forces parallel to the <100> direction family F_f tends toward its minimum. S_f tends to its absolute minimum when the force direction is parallel to <111>. Considering $\left[\frac{S_f}{F_f}\right]^*$, the <111> and the <110> result in absolute and local minima. This corresponds to either a minimum of S_f, or a maximum of F_f. Force directions along the <100> direction are favorable for shear deformation. Along the <100> direction family the force direction can vary by approximately 30° in any direction without resulting in a large decrease of $\left[\frac{S_f}{F_f}\right]^*$. The results of this study indicate that this set of directions should be included in the machining strategy to favor shear deformation and to suppress surface fracture.

4 Conclusions

In this study, the effect of resultant force direction for on-axis single point diamond turning of (100)Ge was investigated. The feedrate ranged from 0.3 μm/rev to 12 μm/rev. The resulting surface topography was characterized by AFM. The Schmid factor S_f and the fracture factor F_f were calculated for all resultant force directions and their ratio $\left[\frac{S_f}{F_f}\right]^*$ was investigated. The $\left[\frac{S_f}{F_f}\right]^*$ ratio was found to predict the cutting direction families that generate fracture. The relationship between $\left[\frac{S_f}{F_f}\right]^*$ and the cutting direction showed that there are

three regimes of (100)Ge during on-axis turning, based on the resultant force angle and corroborated by topography measurements:

- When the resultant force angle is smaller than 40°, fracture is expected for the <110> cutting direction family, as shown by Nakasuji et al. [6].
- When the resultant force angle is between 40° and 55°, fracture is expected for both the <100> and the <110> cutting direction families. This was shown in previous single point diamond turning studies by the authors [10,11] and for the larger feedrates investigated in this study.
- When the resultant force angle is above 55°, fracture is expected for the <100> cutting direction family, as shown for the smaller feedrates investigated in this study.
- Across the full range of possible force directions, $\left[\frac{S_f}{F_f}\right]^*$ indicates that the <110> and <111> force directions favor fracture, while directions near <100> tend to favor slip.

These results indicate that the ratio can be used to predict the onset of fracture in specific cutting directions based on the resultant force angle developed during machining. The ratio could be used to guide the machining strategy of single crystal Ge.

Acknowledgment

The support of this research by NSF grants CMMI-2210365 and CMMI-2210394 is gratefully acknowledged.

References

[1] Yonenaga, I., 2019, "Germanium Crystals," *Single Crystals of Electronic Materials*, Elsevier, pp. 89–127. https://doi.org/10.1016/B978-0-08-102096-8.00004-5.

[2] Kaplunov, I. A., Kolesnikov, A. I., Kropotov, G. I., and Rogalin, V. E., 2019, "Optical Properties of Single-Crystal Germanium in the THz Range," Opt. Spectrosc., **126**(3), pp. 191–194. https://doi.org/10.1134/S0030400X19030093.

[3] Dash, W. C., and Newman, R., 1955, "Intrinsic Optical Absorption in Single-Crystal Germanium and Silicon at 77°K and 300°K," Phys. Rev., **99**(4), pp. 1151–1155. https://doi.org/10.1103/PhysRev.99.1151.

[4] Taishi, T., Ohno, Y., and Yonenaga, I., 2009, "Reduction of Grown-in Dislocation Density in Ge Czochralski-Grown from the B2O3-Partially-Covered Melt," Journal of Crystal Growth, **311**(22), pp. 4615–4618. https://doi.org/10.1016/j.jcrysgro.2009.09.001.

[5] Rolland, J. P., Davies, M. A., Suleski, T. J., Evans, C., Bauer, A., Lambropoulos, J. C., and Falaggis, K., 2021, "Freeform Optics for Imaging," Optica, **8**(2), p. 161. https://doi.org/10.1364/OPTICA.413762.

[6] Nakasuji, T., Kodera, S., Hara, S., Matsunaga, H., Ikawa, N., and Shimada, S., 1990, "Diamond Turning of Brittle Materials for Optical Components," CIRP Annals, **39**(1), pp. 89–92. https://doi.org/10.1016/S0007-8506(07)61009-9.

[7] Owen, J. D., Troutman, J. R., Harriman, T. A., Zare, A., Wang, Y. Q., Lucca, D. A., and Davies, M. A., 2016, "The Mechanics of Milling of Germanium for IR Applications," CIRP Annals, **65**(1), pp. 109–112. https://doi.org/10.1016/j.cirp.2016.04.076.

[8] Zare, A., Tunesi, M., Harriman, T. A., Troutman, J. R., Davies, M. A., and Lucca, D. A., 2023, "Face Turning of Single Crystal (111)Ge: Cutting Mechanics and

Surface/Subsurface Characteristics," Journal of Manufacturing Science and Engineering, **145**(7), p. 071007. https://doi.org/10.1115/1.4057054.

[9] Tunesi, M., Lucca, D. A., Davies, M. A., Zare, A., Gordon, M. C., Sizemore, N. E., and Wang, Y. Q., 2022, "Surface Integrity of Diamond Turned (100)Ge," Procedia CIRP, **108**, pp. 665–669. https://doi.org/10.1016/j.procir.2022.03.103.

[10] Tunesi, M., Sizemore, N. E., Davies, M. A., and Lucca, D. A., 2023, "Effect of Cutting Speed in Single Point Diamond Turning of (100)Ge," Manufacturing Letters, **38**, pp. 15–18. https://doi.org/10.1016/j.mfglet.2023.08.144.

[11] Tunesi, M., Lawing, E., Estes, C., Gasson, J., Dutterer, B. S., Davies, M. A., and Lucca, D. A., 2024, "Effect of Cutting Speed on the Surface Integrity of Single Point Diamond Turned (100)Ge," Procedia CIRP, **123**, pp. 322–327. https://doi.org/10.1016/j.procir.2024.05.057.

[12] Lawing, E., Tunesi, M., Estes, C., Gasson, J., Dutterer, B. S., Lucca, D. A., and Davies, M. A., 2024, "Mechanics and Surface Characterization of High-Speed Diamond Turning of Germanium," Procedia CIRP, **123**, pp. 328–333. https://doi.org/10.1016/j.procir.2024.05.058.

[13] Tunesi, M., Adam, B., Rickens, K., Riemer, O., and Lucca, D. A., 2024, "Effect of Resultant Force Direction in Single Point Diamond Turning of (111)CaF_2," CIRP Journal of Manufacturing Science and Technology, **55**, pp. 411–419. https://doi.org/10.1016/j.cirpj.2024.11.001.

[14] Kwon, S. B., Nagaraj, A., Yoon, H.-S., and Min, S., 2020, "Study of Material Removal Behavior on R-Plane of Sapphire during Ultra-Precision Machining Based on Modified Slip-Fracture Model," Nanotechnology and Precision Engineering, **3**(3), pp. 141–155. https://doi.org/10.1016/j.npe.2020.07.001.

[15] Kwon, S. B., and Min, S., 2024, “Studying Mechanism of Anisotropic Crack Generation on C-, R-, A-, and M-Planes of Sapphire during Ultra-Precision Orthogonal Cutting Using a Visualized Slip/Fracture Activation Model,” Nanotechnology and Precision Engineering, **7**(4), p. 043006. https://doi.org/10.1063/10.0026318.

[16] Tunesi, M., 2025, “Effect of Resultant Force Direction in Single Point Diamond Turning of Brittle Single Crystal Materials,” Oklahoma State University. PhD dissertation.

[17] Schmid, E., Boas, W., 1968, “Plasticity and Strength of Metal Crystals,” *Plasticity of Crystals: With Special Reference to Metals*, Chapman & Hall, pp. 77–226.

[18] Seitz, F., 1952, “The Plasticity of Silicon and Germanium,” Phys. Rev., **88**(4), pp. 722–724. https://doi.org/10.1103/PhysRev.88.722.

[19] Treuting, R. G., 1955, “Some Aspects of Slip in Germanium,” JOM, **7**(9), pp. 1027–1030. https://doi.org/10.1007/BF03377606.

[20] Serbena, F. C., and Roberts, S. G., 1994, “The Brittle-to-Ductile Transition in Germanium,” Acta Metallurgica et Materialia, **42**(7), pp. 2505–2510. https://doi.org/10.1016/0956-7151(94)90331-X.

[21] Gleizer, A., and Sherman, D., 2014, “The Cleavage Energy at Initiation of (110) Silicon,” Int J Fract, **187**(1), pp. 1–14. https://doi.org/10.1007/s10704-013-9882-8.

[22] Jaccodine, R. J., 1963, “Surface Energy of Germanium and Silicon,” J. Electrochem. Soc., **110**(6), p. 524. https://doi.org/10.1149/1.2425806.

[23] Wortman, J. J., and Evans, R. A., 1965, “Young’s Modulus, Shear Modulus, and Poisson’s Ratio in Silicon and Germanium,” Journal of Applied Physics, **36**(1), pp. 153–156. https://doi.org/10.1063/1.1713863.

[24] Semechko, A., 2024, “Suite of Functions to Perform Uniform Sampling of a Sphere.” GitHub, https://github.com/AntonSemechko/S2-Sampling-Toolbox

Figure Caption List

Figure 1. Single point diamond turning configuration indicating (a) the specimen, tool and dynamometer, (b) the forces measured during machining, (c) the geometric cutting parameters, and (d) the rake angle, clearance angle, cutting speed v_c, cutting force F_C and thrust force F_T.

Figure 2. Generation of the directions on a sphere using a triangular surface mesh of an icosahedron.

Figure 3. (a) Optical image and (b) schematic of the (100)Ge specimen after on-axis turning. Red and yellow areas indicate the locations of the lobes where fracture was present. Green areas indicate locations where fracture was not visible. The feedrate decreases from the inside ring to the outside. The colored reflections in the optical image are unavoidable artifacts and should not be considered.

Figure 4. Surface topography measured by AFM on (100)Ge for surfaces turned with feedrates from 0.3 μm/rev to 12 μm/rev. The images are oriented with the cutting direction vertically.

Figure 5. Cutting and thrust force for one revolution of the (100)Ge specimen. The data was selected at the center of each respective band.

Figure 6. Cutting and thrust force averages calculated using 20 revolutions of data. The dashed lines indicate the maximum and the minimum of the forces.

Figure 7. Resultant force angle average calculated using 20 revolutions of data. The dashed lines indicate the maximum and the minimum of the resultant force angle.

Figure 8. S_f, F_f, and $\left[\frac{S_f}{F_f}\right]^*$ for (100)Ge calculated for resultant force angles between 55° and 65°.

Figure 9. (a) 3D surface of $\left[\frac{S_f}{F_f}\right]^*$ for (100)Ge and (b) the values of $\left[\frac{S_f}{F_f}\right]^*$ for a resultant force angle of 55°, 60° and 65° are represented by a section of the 3D surface.

Figure 10. S_f, F_f, and $\left[\frac{S_f}{F_f}\right]^*$ calculated for resultant force angles from 35° to 45°.

Figure 11. (a) 3D surface of $\left[\frac{S_f}{F_f}\right]^*$ for (100)Ge and (b) section of the 3D surface with $\left[\frac{S_f}{F_f}\right]^*$ highlighted for 35°, 40° and 45°. (c) shows the plots of $\left[\frac{S_f}{F_f}\right]^*$ for the same resultant force angles.

Figure 12. S_f, F_f and $\left[\frac{S_f}{F_f}\right]^*$ calculated for single crystal Ge. The colored dots indicate low index directions. Each point on the sphere corresponds to a resultant force direction, defined by the point's coordinates. The color indicates the value of S_f, F_f and $\left[\frac{S_f}{F_f}\right]^*$, mapped on a scale from blue to red for the minimum and maximum values, respectively. All three plots are oriented similarly.

Figures

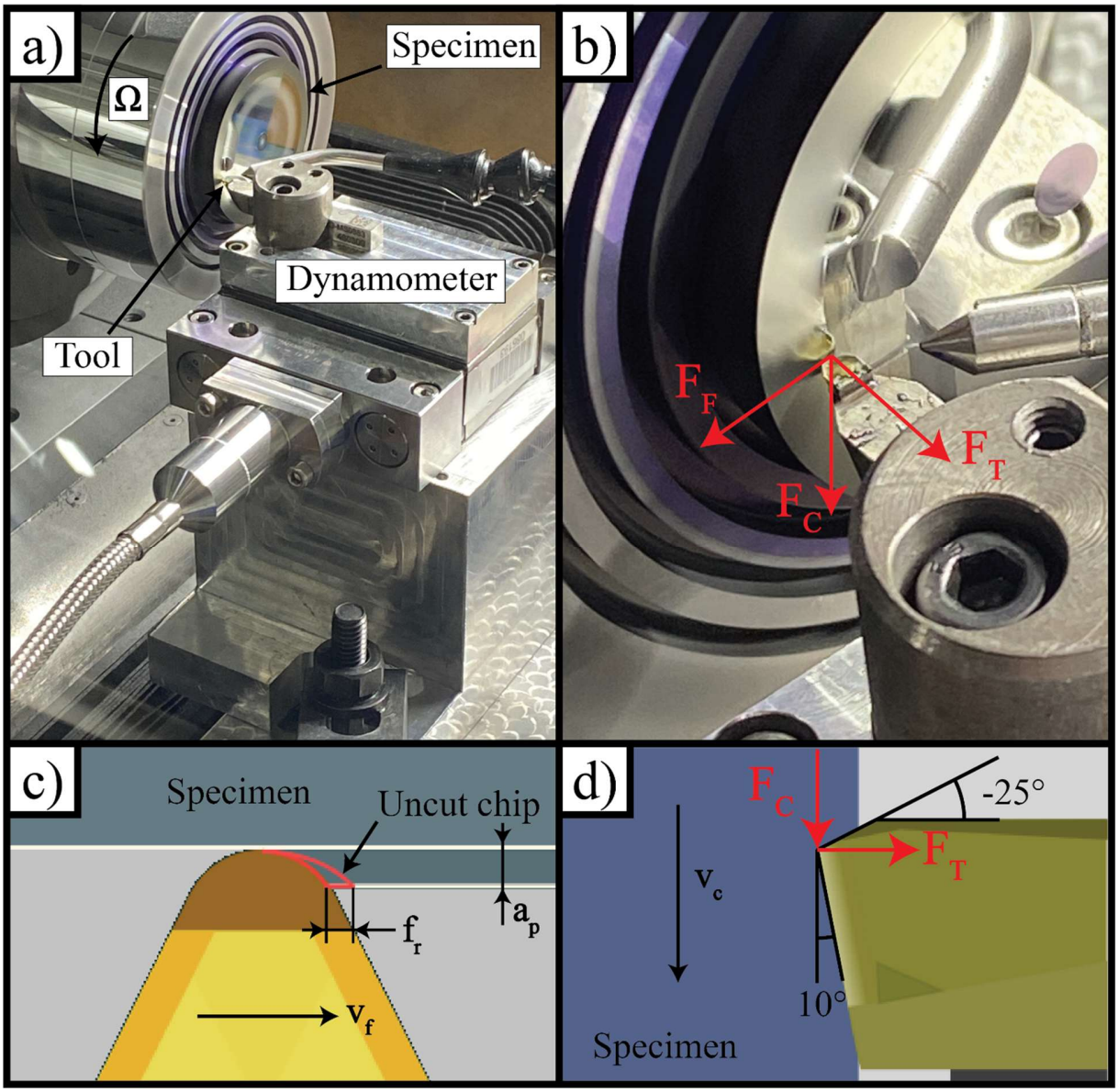

Figure 1. Single point diamond turning configuration indicating (a) the specimen, tool and dynamometer, (b) the forces measured during machining, (c) the geometric cutting parameters, and (d) the rake angle, clearance angle, cutting speed v_c, cutting force F_C and thrust force F_T.

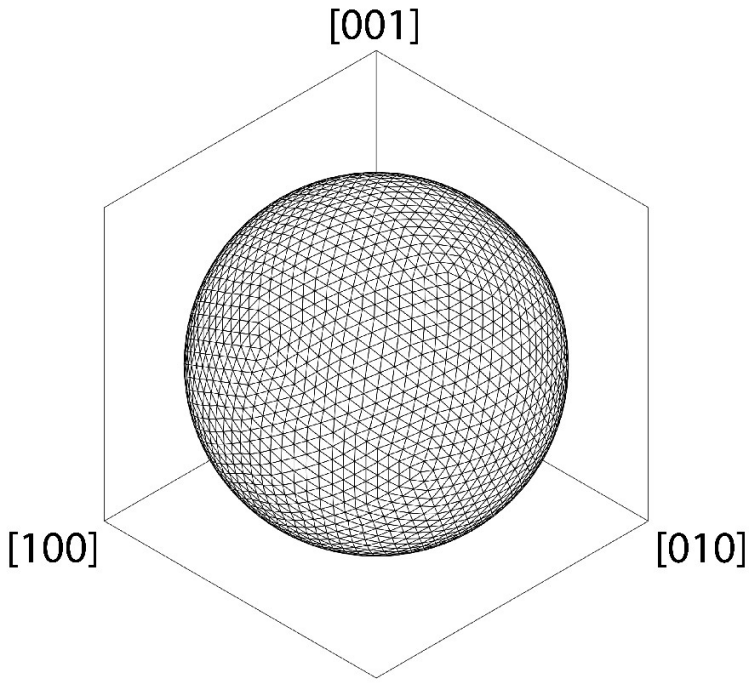

Figure 2. Generation of the directions on a sphere using a triangular surface mesh of an icosahedron.

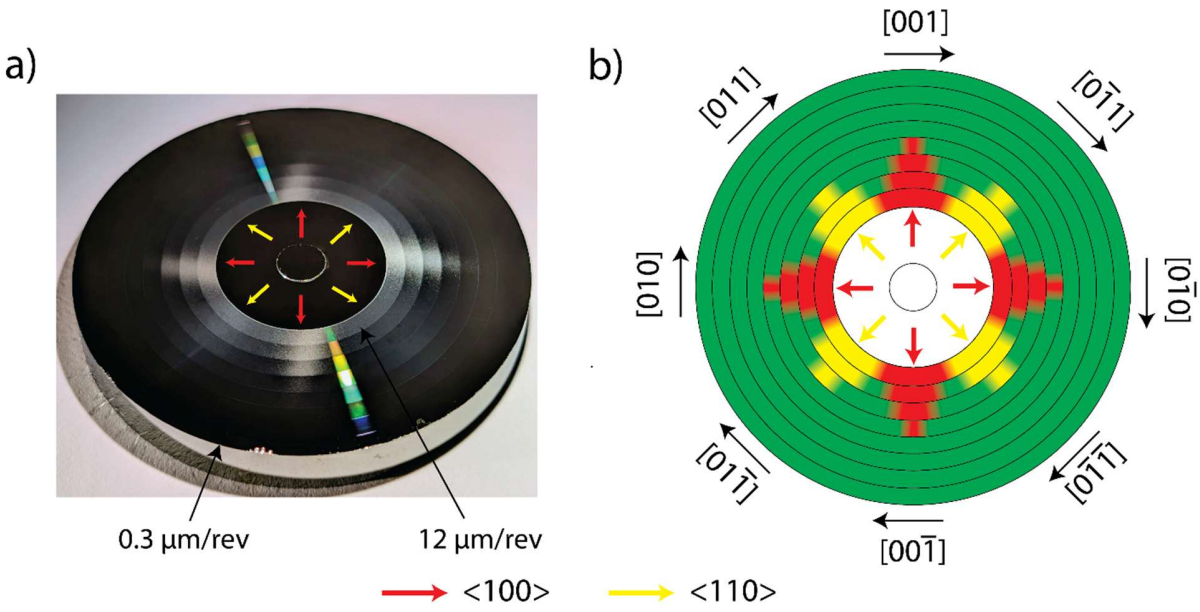

Figure 3. (a) Optical image and (b) schematic of the (100)Ge specimen after on-axis turning. Red and yellow areas indicate the locations of the lobes where fracture was present. Green areas indicate locations where fracture was not visible. The feedrate decreases from the inside ring to the outside. The colored reflections in the optical image are unavoidable artifacts and should not be considered.

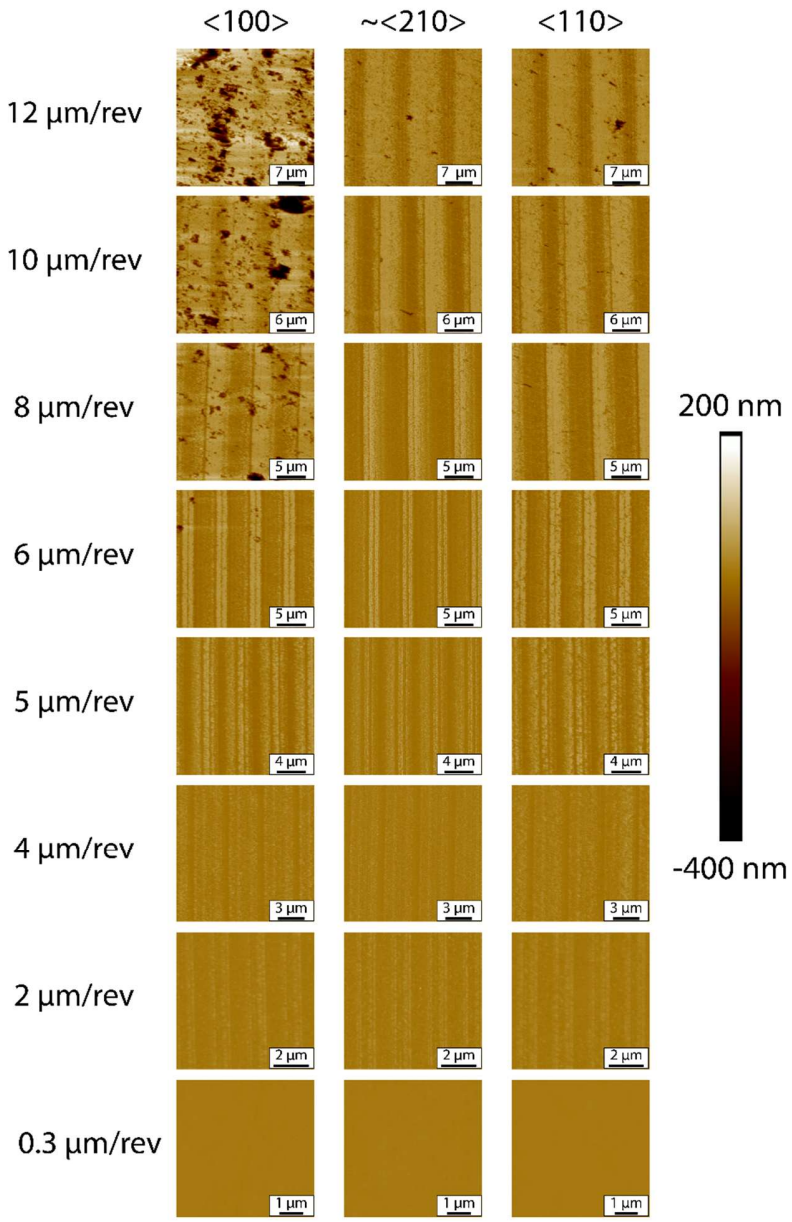

Figure 4. Surface topography measured by AFM on (100)Ge for surfaces turned with feedrates from 0.3 µm/rev to 12 µm/rev. The images are oriented with the cutting direction vertically.

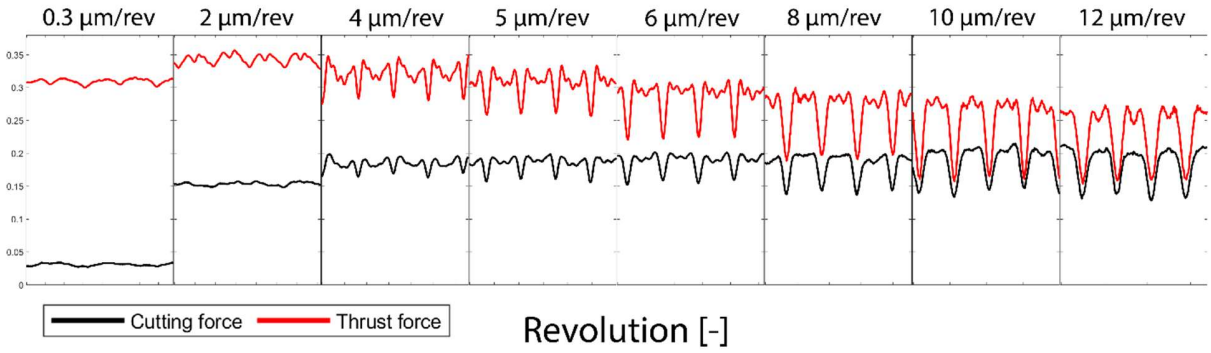

Figure 5. Cutting and thrust force for one revolution of the (100)Ge specimen. The data was selected at the center of each respective band.

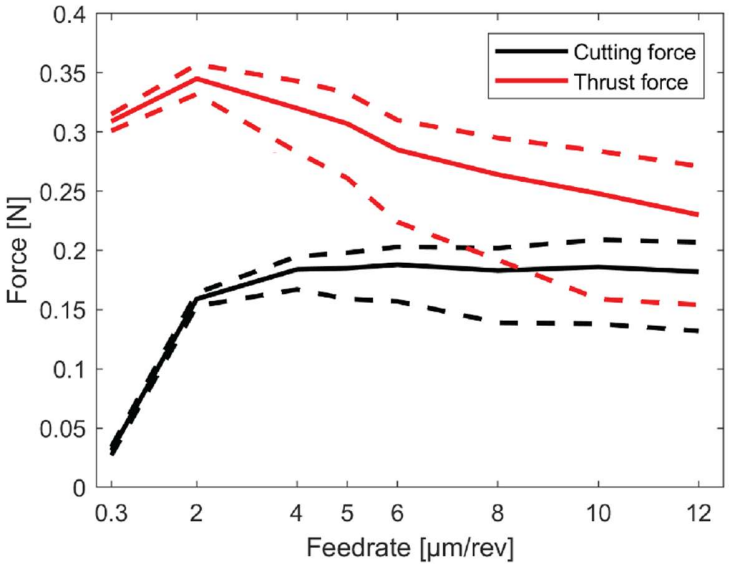

Figure 6. Cutting and thrust force averages calculated using 20 revolutions of data. The dashed lines indicate the maximum and the minimum of the forces.

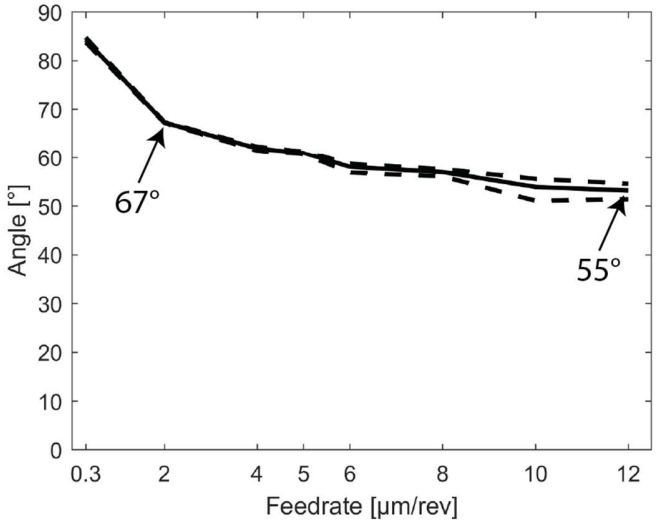

Figure 7. Resultant force angle average calculated using 20 revolutions of data. The dashed lines indicate the maximum and the minimum of the resultant force angle.

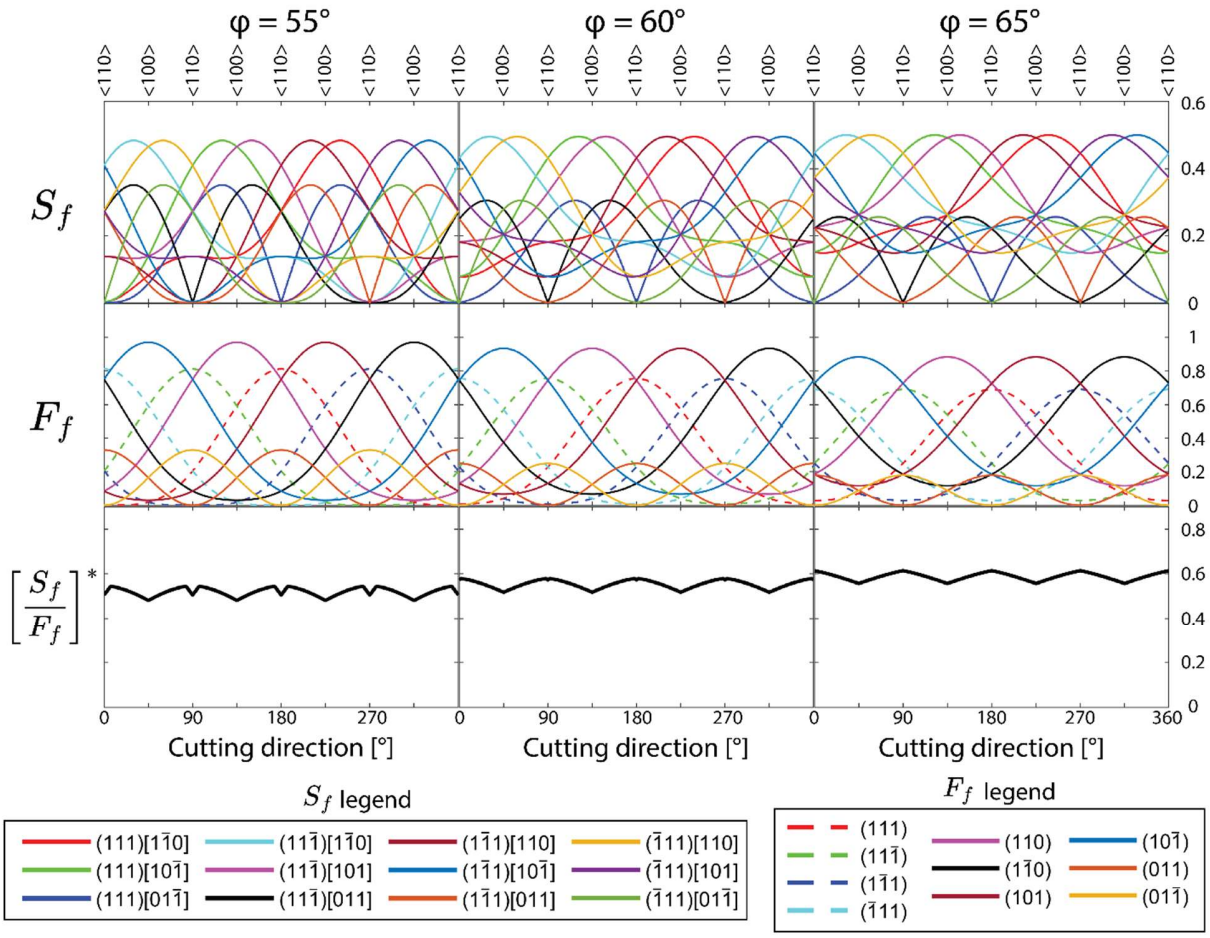

Figure 8. S_f, F_f, and $\left[\frac{S_f}{F_f}\right]^*$ for (100)Ge calculated for resultant force angles between 55° and 65°.

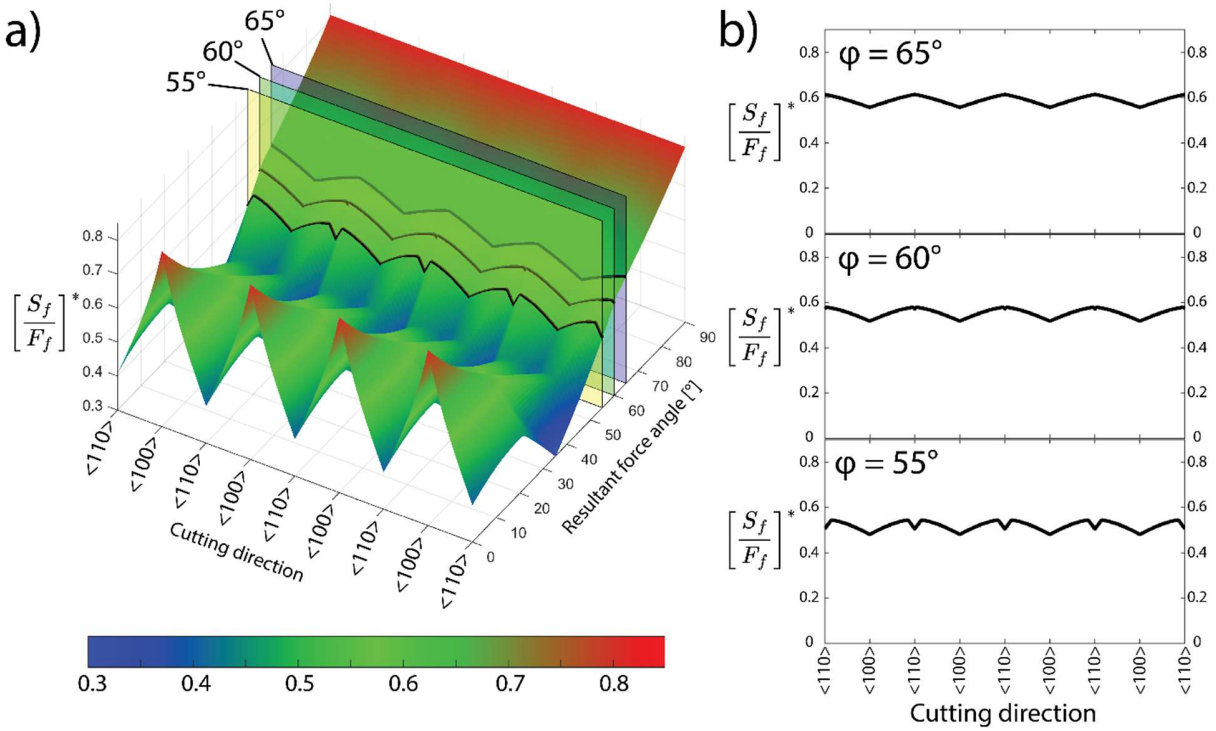

Figure 9. (a) 3D surface of $\left[\frac{S_f}{F_f}\right]^*$ for (100)Ge and (b) the values of $\left[\frac{S_f}{F_f}\right]^*$ for a resultant force angle of 55°, 60° and 65° are represented by a section of the 3D surface.

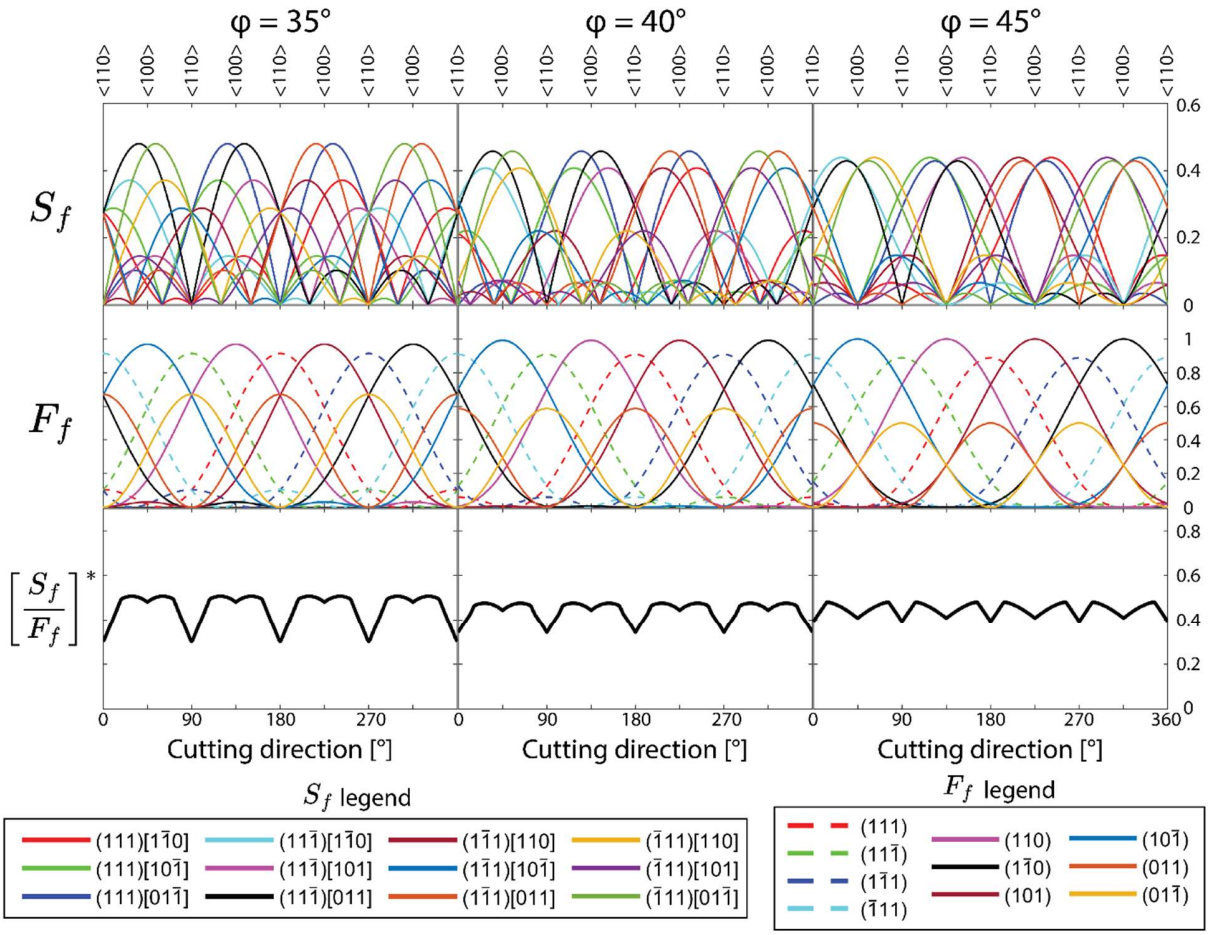

Figure 10. S_f, F_f, and $\left[\frac{S_f}{F_f}\right]^*$ calculated for resultant force angles from 35° to 45°.

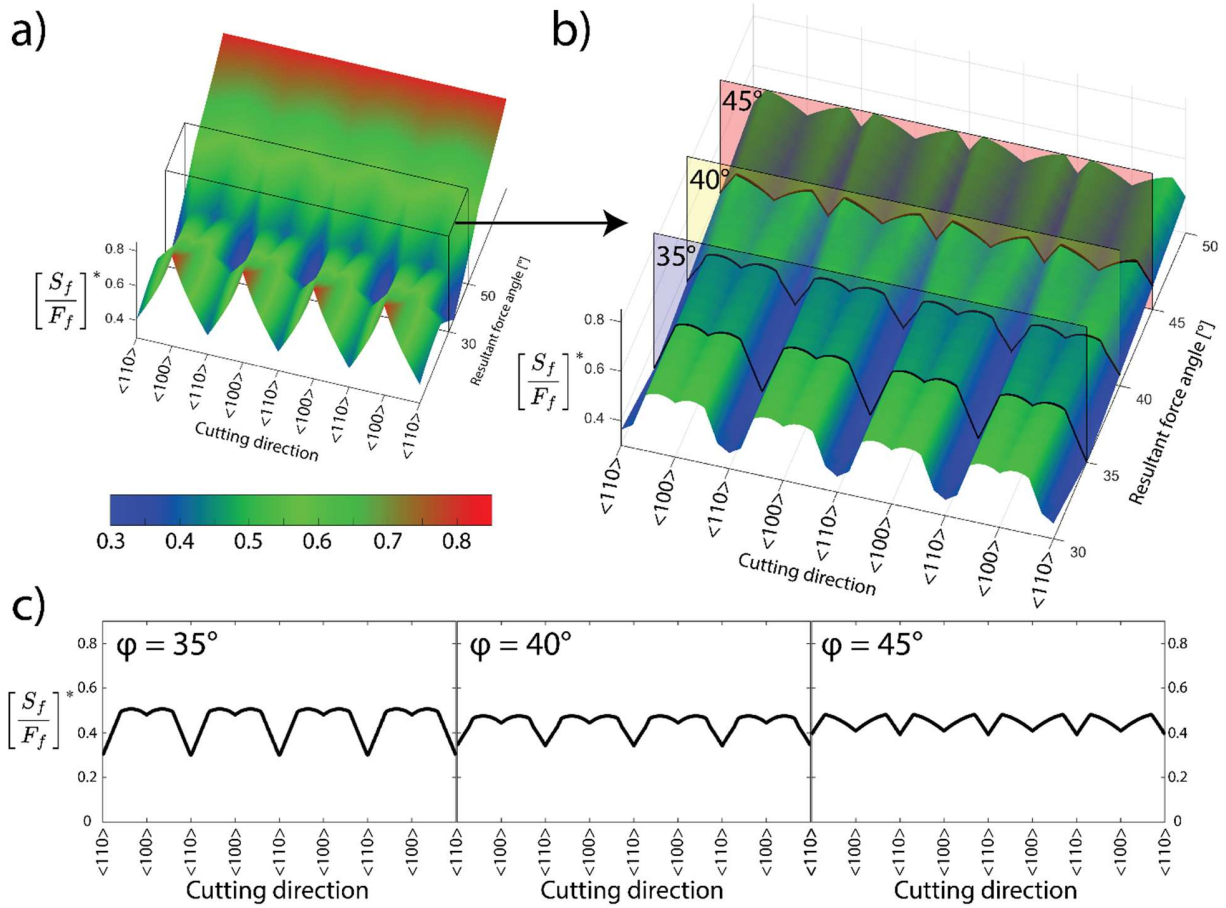

Figure 11. (a) 3D surface of $\left[\frac{S_f}{F_f}\right]^*$ for (100)Ge and (b) section of the 3D surface with $\left[\frac{S_f}{F_f}\right]^*$ highlighted for 35°, 40° and 45°. (c) shows the plots of $\left[\frac{S_f}{F_f}\right]^*$ for the same resultant force angles.

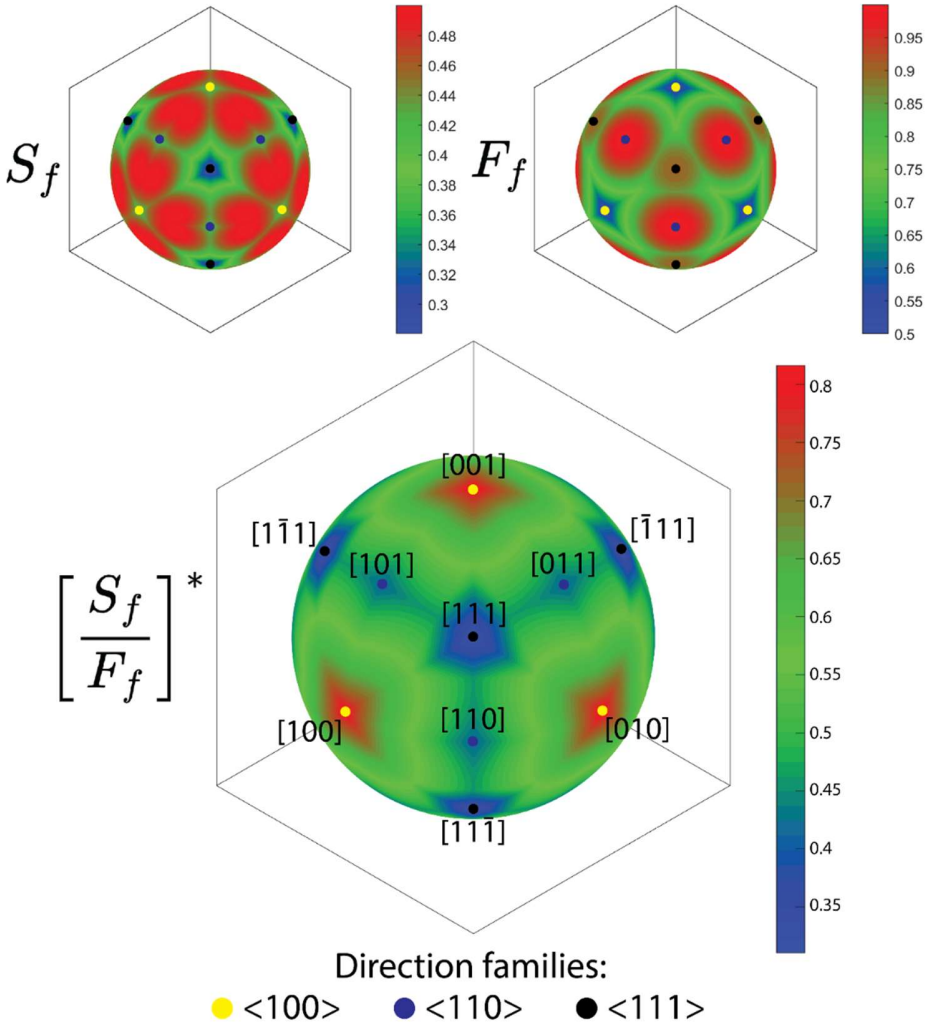

Figure 12. S_f, F_f and $\left[\frac{S_f}{F_f}\right]^*$ calculated for single crystal Ge. The colored dots indicate low index directions. Each point on the sphere corresponds to a resultant force direction, defined by the point's coordinates. The color indicates the value of S_f, F_f and $\left[\frac{S_f}{F_f}\right]^*$, mapped on a scale from blue to red for the minimum and maximum values, respectively. All three plots are oriented similarly.

Tables

Table 1 Single point diamond turning parameters used for the preparation of the Ge specimen and for the turning experiments

Parameter	Preparation	Experiment
Rotational speed [rpm]	2000	Variable
Cutting speed [m/s]	variable	4
Feedrate [μm/rev]	0.3	0.3, 2, 4, 5, 6, 8, 10, 12
Depth of cut [μm]	10	10

Table 2: Slip systems and fracture systems of single crystal Ge used in the calculation of S_f and F_f

Slip systems	Fracture systems
(111)[1-10], (111)[10-1], (111)[01-1], (-111)[110], (-111)[101], (-111)[01-1], (1-11)[110], (1-11)[10-1], (1-11)[011], (11-1)[1-10], (11-1)[101], (11-1)[011],	(111), (-111), (1-11), (11-1) (110), (1-10), (101), (10-1), (011), (01-1)